

**JRC2016-5782**

**FINITE ELEMENT BOND MODELING FOR INDENTED WIRES IN PRETENSIONED  
CONCRETE CROSSTIES**

**Hailing Yu and David Jeong**

Structures and Dynamics Division

John A. Volpe National Transportation Systems Center

U.S. Department of Transportation

Cambridge, MA 02142, U.S.A.

**ABSTRACT**

Indented wires have been increasingly employed by concrete crosstie manufacturers to improve the bond between prestressing steel reinforcements and concrete, as bond can affect several critical performance measures, including transfer length, splitting propensity and flexural moment capacity of concrete ties. While extensive experimental testing has been conducted at Kansas State University (KSU) to obtain bond characteristics of about a dozen commonly used prestressing wires, this paper develops macro-scale or phenomenological finite element bond models for three typical wires with spiral or chevron indent patterns. The steel wire-concrete interface is homogenized and represented with a thin layer of cohesive elements sandwiched between steel and concrete elements. The cohesive elements are assigned traction-displacement constitutive or bond relations that are defined in terms of normal and shear stresses versus interfacial dilatation and slip within the elasto-plastic framework. A yield function expressed in quadratic form of shear stress and linear form of normal stress is adopted. The yield function takes into account the adhesive mechanism and hardens in the post-adhesive stage. The plastic flow rule is defined such that the plastic dilatation evolves with the plastic slip. The mathematical forms of the yield and plastic flow functions are the same for all three wire types, but the bond parameters are specific for each wire. The adhesive, hardening and dilatational bond parameters are determined for each wire type based on untensioned pullout tests and pretensioned prism tests conducted at KSU. Simulation results using these bond models are further verified with surface strain data measured on actual concrete crossties made with the three respective prestressing wires at a tie manufacturing plant.

**INTRODUCTION**

Concrete crossties are made by embedding prestressing steel reinforcements in concrete and releasing the pretension in the reinforcements once desired concrete strength is achieved. The interaction between steel reinforcements and concrete, commonly referred to as bond, affects several important aspects of concrete tie performance, including transfer length, bursting or splitting propensity, and flexural moment capacity. Under in-track service loads, concrete crossties have displayed several failure modes that have led to premature replacement of track components and sometimes derailment accidents [1]. Improving the bond quality between steel reinforcements and concrete can potentially mitigate or even prevent some of these failures.

Concrete tie manufacturers have increasingly employed indented steel reinforcement wires to improve bond. Increased bond can shorten the transfer length needed to transfer the prestressing force from the steel reinforcement to the concrete. However, indented wires tend to increase the dilatational effect along the steel-concrete interface, and concrete surrounding indented wires are more likely to develop bursting/splitting cracks. Furthermore, bond is believed to affect the ultimate flexural moment capacity of concrete ties prior to failure. Under the sponsorship of the Federal Railroad Administration (FRA), Kansas State University (KSU) conducted extensive bond testing and transfer length measurement and analysis on 15 selected prestressing wires and strands for concrete crossties [2-5]. Figure 1 show microscopic surface images of four typical wires and a seven-wire strand used in the KSU testing program and their 3D models produced by a precision non-contact profilometer [6].

The Volpe Center has been developing a finite element (FE) analysis framework for pretensioned concrete crossties. Bond modeling is a key component in this analysis framework. An

important objective of Volpe Center's ties and fasteners research, also sponsored by the FRA, is to develop realistic concrete tie models, including FE bond models for various reinforcement interfaces, and apply the models in predicting and evaluating critical concrete tie performance. The authors previously developed elasto-plastic FE bond models for the smooth wire WA [7] and the seven-wire strand SA [8], and these models were calibrated and validated with KSU's bond testing and transfer length measurement data. The bond models for the seven-wire strand were further applied to evaluate the center negative flexural performance of concrete ties found in a derailment accident [8-9].

This paper continues the bond modeling work and develops macro-scale or phenomenological FE bond models for the three indented wires shown in Figure 1: WE, WG and WH. Together with the smooth wire WA, wires WE, WG and WH provide a representative range of bond behavior studied with the untensioned pullout tests at KSU [2].

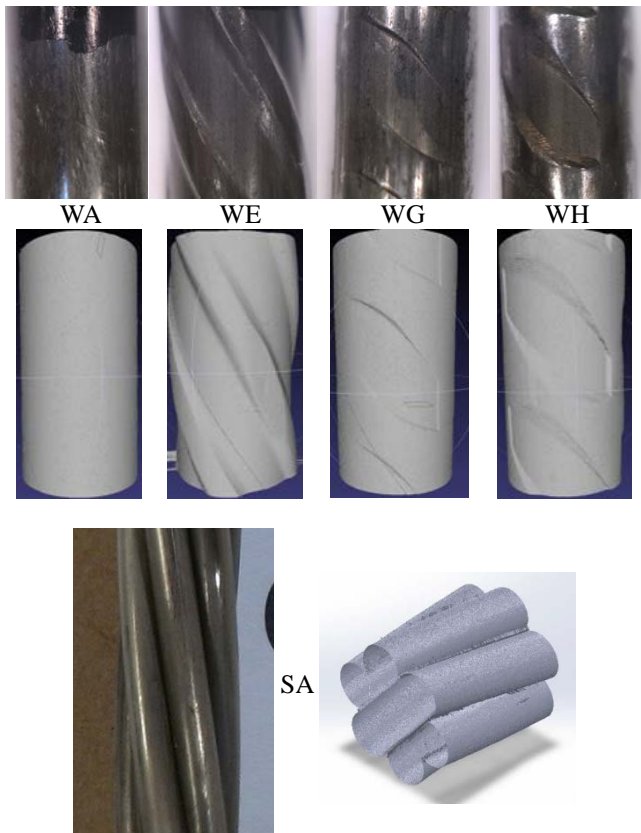


**Figure 1: Microscopic images of wires WA, WE, WG, WH and strand SA studied by KSU researchers [2-5], and their 3D models produced by a precision non-contact profilometer [6].**

The primary bond mechanisms of indented wires are adhesion, mechanical interaction and friction. Figure 2 illustrates the micromechanics along an indented wire-concrete interface. The steel wire is initially pretensioned with a traction

$t_0$ . When the traction is reduced by  $\Delta t$  at one end of the wire in a pretension release process, the wire slips relative to the surrounding concrete and dilates radially due to Hoyer effect. In addition, the surface indent of the wire initially interlocks with the matching inner surface of the concrete, but when the wire and concrete surfaces slip relative to each other, the surfaces become mismatched and produce additional normal dilation (or dilatation) along the steel-concrete interface. The interface dilatation strengthens the bonding between the steel reinforcements and concrete, but it also applies radial (or normal) pressure on the concrete's inner wall. Sufficiently large normal pressure can split the concrete longitudinally, leading to bursting failure of concrete crossties. In the macro-scale bond modeling adopted in this study, the surface indents are homogenized and represented with a thin interface layer sandwiched between the steel wire and the concrete. A phenomenological bond model is expected to reproduce the slip and dilatational effects even with the homogenized interface.

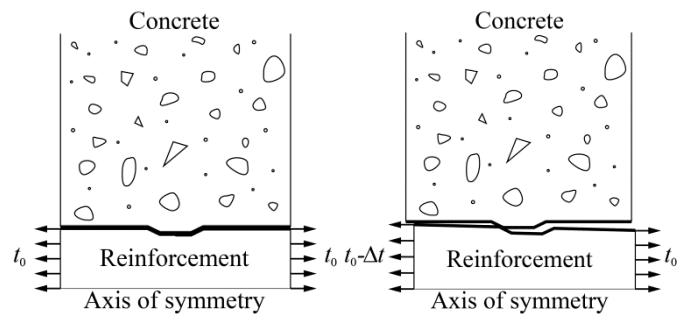


**Figure 2: Micromechanics in the indented wire-concrete interface: relative slip and dilatation as the concrete tie changes from the pretensioned (left) to the pretension released phase (right).**

This paper presents the development, calibration and validation of FE bond models for the three indented wires shown in Figure 1. First, the elasto-plastic framework for bond modeling is described. The governing equations, solution approach, yield function and plastic flow rule are presented or defined, and the bond parameters are identified. Second, calibration of the bond parameters is carried out based on untensioned pullout tests and pretensioned prism tests conducted on concrete specimens at KSU. One set of bond parameters are determined for each of the three indented wires. Third, simulation results from the calibrated bond models are verified with surface strain data measured on actual concrete crossties made at a tie manufacturing plant. Last, a summary of the work and main conclusions are presented. A schematic of the FEA framework employed in this paper is shown in Figure 3.

Applications of the presented bond models are not shown here, but a separate paper [10] applies the bond models to predict concrete tie deflection profiles under various reinforcement, geometry, loading and support conditions. Such information can be useful for assessing deteriorated conditions in the concrete tie-ballast interface.

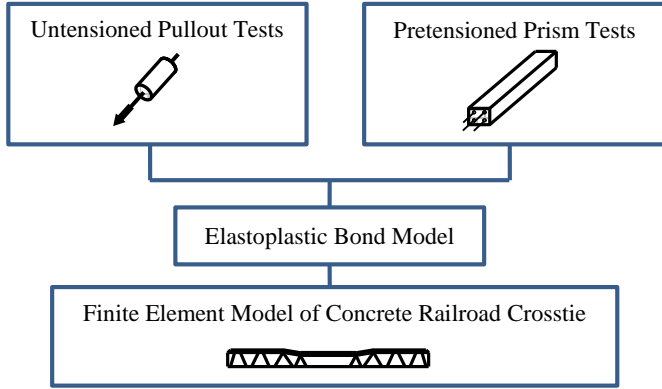


Figure 3: FEA framework employed in this study.

### ELASTOPLASTIC BOND MODELING APPROACH

The commercial FE analysis software Abaqus was employed in this study [11]. The concrete material was modeled with concrete damaged plasticity, and the modeling framework and material parameter calibration were described in detail in previous publications [12-13]. The elasto-plastic bond model development in this paper follows the general plasticity theory and FE procedure described by Zienkiewicz and Taylor [14]. User subroutines were written for both axisymmetric and 3D cohesive elements in Abaqus, but only the 3D governing equations, similar to the theoretical basis for frictional contact developed by Michalowski and Mroz [15], are presented here. The same framework was previously employed in modeling the bond for the smooth wire [7] and the seven-wire strand [8]. All analyses were conducted statically.

### Governing Equations

Figure 4 shows the local coordinate system defined for a 3D cohesive element [11]. It includes a normal (or thickness) direction and two shear directions, depicted by unit vectors  $\mathbf{n}$ ,  $\mathbf{s}$  and  $\mathbf{t}$ , respectively. The traction-displacement constitutive relation type is adopted. The interface stress tensor  $\boldsymbol{\sigma}$  includes a normal component  $\sigma$  and two shear components  $\tau_1$  and  $\tau_2$ ,

$$\boldsymbol{\sigma} = \sigma \mathbf{n} + \tau_1 \mathbf{s} + \tau_2 \mathbf{t} \quad (1)$$

The magnitude of the total shear stress is

$$|\boldsymbol{\tau}| = \sqrt{\tau_1^2 + \tau_2^2} \quad (2)$$

The interface displacement tensor  $\mathbf{u}$  includes dilation  $u_n$  and slips  $u_{t1}$  and  $u_{t2}$

$$\mathbf{u} = u_n \mathbf{n} + u_{t1} \mathbf{s} + u_{t2} \mathbf{t} \quad (3)$$

which can be decomposed into elastic and plastic components

$$\mathbf{u} = \mathbf{u}^{el} + \mathbf{u}^{pl} \quad (4)$$

This material is declared a work of the U.S. Government and is not subject to copyright protection in the United States. Approved for public release; distribution is unlimited.

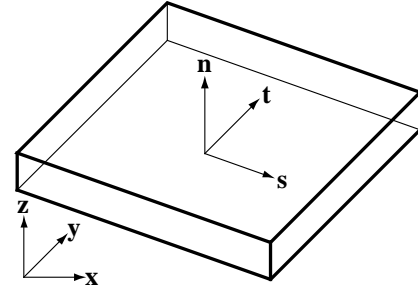


Figure 4: Local coordinate system ( $\mathbf{n}$ ,  $\mathbf{s}$ ,  $\mathbf{t}$ ) for a 3D cohesive element [11].

The magnitude of the total plastic slip is written as

$$|u_t^{pl}| = \sqrt{(u_{t1}^{pl})^2 + (u_{t2}^{pl})^2} \quad (5)$$

Elasticity of the interface material indicates

$$\boldsymbol{\sigma} = \mathbf{D}^e \mathbf{u}^{el} = \mathbf{D}^e (\mathbf{u} - \mathbf{u}^{pl}) \quad (6)$$

where  $\mathbf{D}^e$  is the elastic matrix with the dimension force/length<sup>3</sup>. Assuming uncoupled elastic normal-shear behavior, we have  $\mathbf{D}^e$  in the following matrix form

$$\mathbf{D}^e = \begin{bmatrix} D_{nn}^e & 0 & 0 \\ 0 & D_{ns}^e & 0 \\ 0 & 0 & D_{nt}^e \end{bmatrix} \quad (7)$$

where the normal ( $D_{nn}^e$ ) and shear elastic stiffness ( $D_{ns}^e$ ,  $D_{nt}^e$ ) are the only non-trivial components. Isotropy in the shear plane further implies  $D_{ns}^e = D_{nt}^e$ .

For elastic loading and unloading, the yield function  $F$  satisfies

$$F < 0 \quad (8)$$

When plastic loading occurs, the stress tensor stays on the yield surface

$$F = 0 \quad (9)$$

The plastic flow rate can be calculated from the plastic potential  $Q$  as follows

$$d\mathbf{u}^{pl} = d\lambda \frac{\partial Q}{\partial \boldsymbol{\sigma}} \quad (10)$$

where  $d\mathbf{u}^{pl}$  is the rate of the plastic interface displacement, and  $d\lambda$  is a proportionality constant. Eq. (10) implies an associated flow rule when  $Q=F$  and a non-associated flow rule when  $Q \neq F$ .

An examination of the bond-slip curves obtained in the unensioned pullout tests on concrete specimens made with the three indented wires WE, WG and WH [2] determined that the yield function may take the following form

$$F = \sigma + H(\tau_1^2 + \tau_2^2 - a^2) \quad (11)$$

where  $a$  is the adhesive strength and  $H$  the hardening parameter. The plastic potential  $Q$  can be further defined as

$$Q = |\tau| + \sigma \tan \psi \quad (12)$$

where  $\psi$  is the dilatational angle and  $\tan \psi$  the dilatational coefficient. If we further denote

$$\mu_d = \tan \psi \quad (13)$$

then Eq. (12) is rewritten as

$$Q = |\tau| + \mu_d \sigma \quad (14)$$

Applying Eq. (14) to Eq. (10) yields the following plastic flow rules

$$du_n^{pl} = \mu_d |du_t^{pl}| \quad (15)$$

$$\frac{du_{t1}^{pl}}{du_{t2}^{pl}} = \frac{\tau_1}{\tau_2} \quad (16)$$

Eq. (15) indicates that the interface's plastic dilatation rate is scaled with the plastic slip rate by a factor of  $\mu_d$ .

A form of the adhesive strength  $a$  depending linearly on the total plastic slip  $|u_t^{pl}|$  is chosen,

$$a = \begin{cases} a_0 \left( 1 - \frac{|u_t^{pl}|}{u_{tc}^{pl}} \right), & \text{if } |u_t^{pl}| \leq u_{tc}^{pl} \\ 0, & \text{if } |u_t^{pl}| > u_{tc}^{pl} \end{cases} \quad (17)$$

where  $a_0$  is the initial adhesive strength and  $u_{tc}^{pl}$  the plastic slip at which adhesion (or cohesion) is first broken completely.

The following form is assumed for the hardening parameter  $H$

$$H = \begin{cases} H_0, & \text{if } |u_t^{pl}| \leq u_{tc}^{pl} \\ H_0 + \frac{H_1 - H_0}{u_{ts}^{pl} - u_{tc}^{pl}} (|u_t^{pl}| - u_{tc}^{pl}), & \text{if } u_{tc}^{pl} < |u_t^{pl}| \leq u_{ts}^{pl} \\ H_1, & \text{if } |u_t^{pl}| > u_{ts}^{pl} \end{cases} \quad (18)$$

where  $H_0$  and  $H_1$  are initial and ultimate hardening parameters, respectively, and  $u_{ts}^{pl}$  the plastic slip at which an ultimate sliding stage is reached. The hardening parameters are therefore constants at the adhesive and sliding stages and linearly varying with the total plastic slip between the two stages.

The dilatational coefficient  $\mu_d$  is further assumed to take the following form

$$\mu_d = \begin{cases} \mu_d^{\max}, & \text{if } |u_t^{pl}| \leq u_{td}^{pl} \\ \frac{\mu_d^{\max}}{u_{td}^{pl} - u_{ts}^{pl}} (|u_t^{pl}| - u_{ts}^{pl}), & \text{if } u_{td}^{pl} < |u_t^{pl}| \leq u_{ts}^{pl} \\ 0, & \text{if } |u_t^{pl}| > u_{ts}^{pl} \end{cases} \quad (19)$$

where  $\mu_d^{\max}$  is the maximum dilatational coefficient and  $u_{td}^{pl}$  the plastic slip at which  $\mu_d$  starts to decrease linearly from  $\mu_d^{\max}$  until reaching 0 at  $u_{ts}^{pl}$ .

Figure 5 shows the plots of  $a$ ,  $H$  and  $\mu_d$  as functions of the plastic slip  $u_t^{pl}$ . Figure 6 shows the yield surfaces and the plastic flow rule. The yield surfaces are defined in quadratic form of the shear stress and linear form of the normal stress, and the shape changes as the hardening parameter evolves. The plastic flow vector for a dilatational interface is assumed to form a dilatational angle  $\psi$  with the  $\tau$ -axis. The dilatational angle evolves with the plastic slip. Table 1 summarizes the bond model parameters which are specific for reinforcement types and need to be determined as such. It is noted that bond parameters within or slightly beyond the adhesive stage (i.e.,  $|u_t^{pl}|$  within or slightly beyond  $u_{tc}^{pl}$ ) are most significant in depicting the bond behavior studied in this paper.

### Local Iteration

At the element level, updated stress  $\sigma$  is sought with given initial stress  $\sigma_0$ , initial displacement  $\mathbf{u}_0$  and incremental displacement  $d\mathbf{u}$ . This can be achieved by solving the following equation involving the residual function  $\mathbf{R}$ ,

$$\mathbf{R} = \mathbf{0} \quad (20)$$

which can be defined according to the plastic loading condition and the plastic flow rules. For the bond model described above, the residual function is written based on Eq. (9) and Eqs. (15-16) as

$$\mathbf{R} = \begin{Bmatrix} F \\ \mu_d |du_t^{pl}| - du_n^{pl} \\ \tau_2 du_{t1}^{pl} - \tau_1 du_{t2}^{pl} \end{Bmatrix} \quad (21)$$

The plastic displacement rate  $d\mathbf{u}^{pl}$  in Eq. (21) can be calculated from the rate form of the elasticity equation Eq. (6)

$$d\mathbf{u}^{pl} = d\mathbf{u} - \mathbf{C}^e d\boldsymbol{\sigma} \quad (22)$$

where  $\mathbf{C}^e$  is the elastic compliance matrix

$$\mathbf{C}^e = \mathbf{D}^{e-1} \quad (23)$$

Eq. (20) is solved by applying the Newton-Raphson method and performing the following substitutive iterations at the element material level until convergence is achieved,

$$\boldsymbol{\sigma}_{i+1} = \boldsymbol{\sigma}_i - \left( \frac{\partial \mathbf{R}}{\partial \boldsymbol{\sigma}} \right)_i^{-1} \mathbf{R}_i \quad (24)$$

where the subscripts “ $i$ ” and “ $i+1$ ” indicate the iteration sequence numbers. Convergence is considered to be achieved when the norm of the vector  $\mathbf{R}$  is sufficiently small.

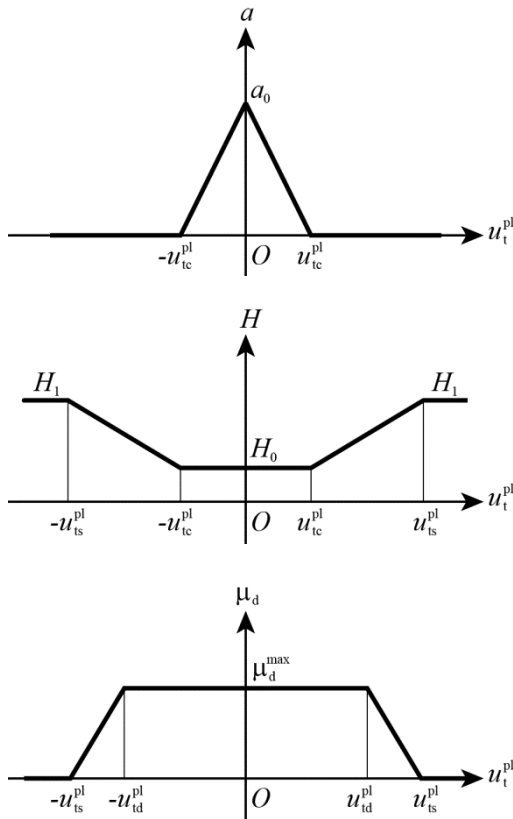


**Figure 5: Adhesive strength, hardening parameter and dilatational coefficient as functions of plastic slip.**

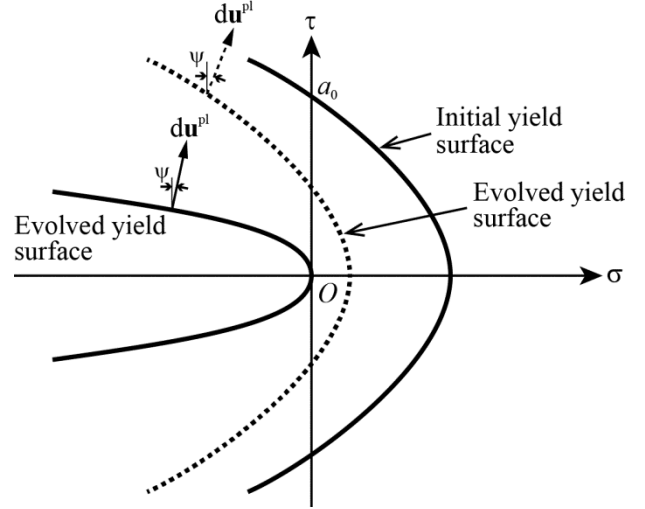


**Figure 6: Yield surfaces and plastic flow rule.**

**Table 1. Bond model parameter nomenclature.**

$D_{nn}^e$	Normal elastic stiffness
$D_{ns}^e (= D_{nt}^e)$	Shear elastic stiffness
$u_{tc}^{pl}$	Plastic slip at which adhesive (or cohesive) stage ends
$u_{td}^{pl}$	Plastic slip at which dilatational coefficient starts to decrease
$u_{ts}^{pl}$	Plastic slip at which sliding stage starts
$a_0$	Initial adhesive strength
$H_0$	Initial hardening parameter
$H_1$	Ultimate hardening parameter
$\mu_d^{max}$	Maximum dilatational coefficient

### Global Stiffness Matrix

In incremental FE analyses, the user material’s Jacobian matrix  $\mathbf{D}^{ep}$  is sought to determine the stress increment  $d\boldsymbol{\sigma}$  in terms of the displacement increment  $d\mathbf{u}$ ,

$$d\boldsymbol{\sigma} = \mathbf{D}^{ep} d\mathbf{u} \quad (25)$$

This element stiffness matrix is passed on to assemble the stiffness matrix used in the global iterations and therefore also referred to as the global stiffness matrix of the element.

By enforcing the consistency condition for plastic loading when the yield function  $F$  takes the form in Eq. (11)

$$dF = \left( \frac{\partial F}{\partial \boldsymbol{\sigma}} \right)^T d\boldsymbol{\sigma} + \frac{\partial F}{\partial H} dH + \frac{\partial F}{\partial a} da = 0 \quad (26)$$

$\mathbf{D}^{ep}$  can be obtained as follows

$$\mathbf{D}^{ep} = \mathbf{D}^e - \frac{\mathbf{D}^e \frac{\partial Q}{\partial \boldsymbol{\sigma}} \left( \frac{\partial F}{\partial \boldsymbol{\sigma}} \right)^T \mathbf{D}^e}{\left( \frac{\partial F}{\partial \boldsymbol{\sigma}} \right)^T \mathbf{D}^e \frac{\partial Q}{\partial \boldsymbol{\sigma}} - \left[ \frac{\partial F}{\partial H} \left( \frac{\partial H}{\partial \mathbf{u}^{pl}} \right)^T + \frac{\partial F}{\partial a} \left( \frac{\partial a}{\partial \mathbf{u}^{pl}} \right)^T \right] \frac{\partial Q}{\partial \boldsymbol{\sigma}}} \quad (27)$$

## CALIBRATION OF BOND MODEL PARAMETERS

The KSU untensioned pullout and pretensioned concrete prism test data [2-3] were employed to calibrate the bond model parameters listed in Table 1.

Figure 7 shows the setup of the untensioned pullout test. The wire has a nominal diameter of 0.209 in. (5.32 mm) and is embedded in a concrete matrix with a 6 in. (152.4 mm) embedment length and a 2 in. (50.8 mm) bond breaking length. The steel tube encasing the concrete specimen has an inner diameter of 4 in. (101.6 mm). The pullout force and the displacements at the unloaded and loaded ends of the steel wire were recorded. Axisymmetric models were developed to simulate this test.

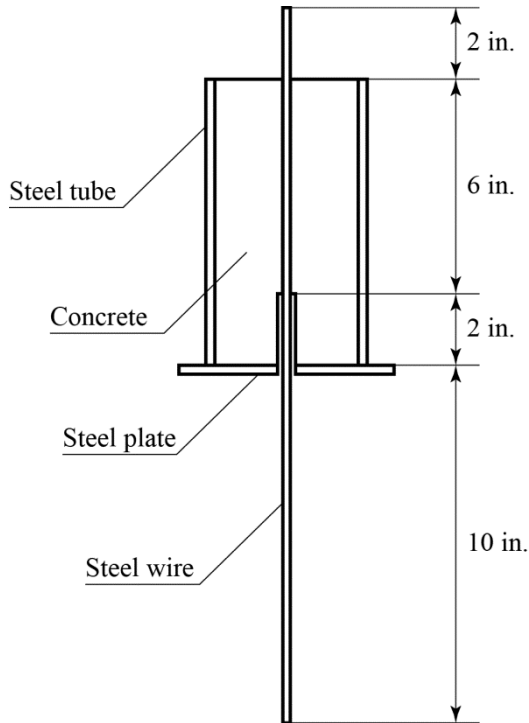


**Figure 7: Illustration of un-tensioned pullout test conducted on a concrete specimen with an indented wire.**

Figure 8 shows the cross section of the concrete prism used in the pretensioned concrete prism test. There are four indented wires embedded in the concrete matrix. The prism measures 3.5 in. (88.9 mm) on each side of its cross section and 69 in. (1.75 m) in length, and every two wires are spaced 1.5 in. (38.1 mm) apart. The wires in the concrete prisms were pretensioned to 7,000 pound force (31,137 N), equivalent to a nominal initial

tensile stress of 203 ksi (1,399.6 MPa). Once the concrete reached a desired compressive strength, the pretension was released with the wires cut at the prism ends. The concrete prisms were tested with three release strengths: 3,500, 4,500 and 6,000 psi (24.1, 31.0 and 41.4 MPa), but simulations of the tests considered only data corresponding to a concrete release strength of 6,000 psi (41.4 MPa). Concrete surface strains were then measured for each prism and used to calculate the transfer length. In modeling, quarter symmetry in the cross section and half symmetry over the length were assumed, resulting in one-eighth of the prism being modeled.

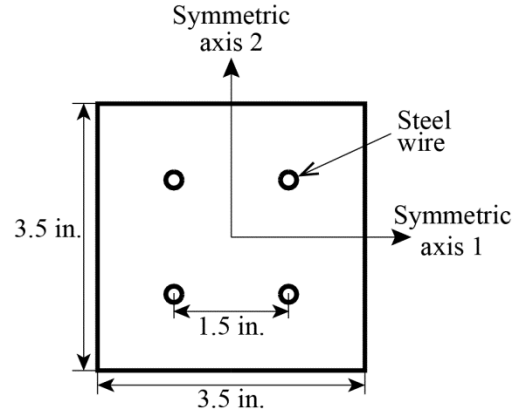


**Figure 8: Illustration of the cross section of a pretensioned concrete prism embedded with indented wires.**

The measurements of concrete surface strain in prism tests were consistently higher than FE predictions. It was reported that due to logistic reasons, concrete strains could not be measured at the same time the wire pretension was released, and the time lapse between the two events led to considerable concrete creep by the time the strain measurements were taken. To be able to make meaningful comparisons between the test data and the simulation results, the following method was developed to account for the added strains due to creep.

Bazant and Baweja [16] postulated that for a constant uniaxial stress  $\sigma$  within the service range and applied at age  $t'$ , the strain  $\varepsilon$  at age  $t$  can be written as

$$\varepsilon(t) = J(t, t')\sigma + \varepsilon_{sh}(t) + \alpha\Delta T(t) \quad (28)$$

where  $J$  is the compliance function,  $\varepsilon_{sh}$  the shrinkage strain,  $\alpha$  the thermal expansion coefficient, and  $\Delta T$  the temperature change. The compliance function can be further expressed in elastic and creep terms as

$$J(t, t') = 1/E(t') + C_0(t, t') + C_d(t, t', t_0) \quad (29)$$

where  $E(t')$  is the modulus of elasticity at loading age  $t'$ ,  $C_0(t, t')$  is the basic creep compliance, and  $C_d(t, t', t_0)$  is the creep compliance due to simultaneous drying. Considering only the basic creep mechanism, we rewrite Eq. (28) as

$$\varepsilon(t) = \sigma/E(t') + \sigma C_0(t, t') \quad (30)$$

If we further assume that at age  $t'$

$$\sigma = E(t')\varepsilon(t') \quad (31)$$

then we can obtain an estimate of  $C_0(t, t')$  as follows,

$$C_0(t, t') = \frac{\varepsilon(t) - \varepsilon(t')}{E(t')\varepsilon(t')} \quad (32)$$

In our post-FE data analyses, we substituted  $\varepsilon(t)$  for the average maximum test measurement and  $\varepsilon(t')$  for the average maximum FE prediction to obtain an estimation of  $C_0$ . Creep adjusted strains were then calculated according to Eq. (30) and compared with the measured strain data.

Table 2 shows the concrete and steel material parameters used in the simulations of the tests. For untensioned pullout tests, the predicted bond stress vs. unloaded ends slip curves were compared with the corresponding test data. For pretensioned prism tests, the predicted concrete surface strain profiles adjusted with creep strain were compared with the corresponding test data. Bond model parameters (Table 1) were initially assigned and iteratively adjusted until simulation results compared favorably with the corresponding test data for both untensioned pullout tests and pretensioned prism tests. The calibrated bond model parameters are shown in Table 3 for all three indented wires, WE, WG and WH.

Figure 9 shows the bond stress-unloaded end slip plots for all three indented wires. The bond stress was calculated as the pullout force divided by the nominal cross sectional area of the wires. The test data were averaged over six specimens.

Figure 10 compares the concrete surface strain profiles in the prism tests. The simulation results were FE predictions with creep strain adjustments described above. The estimated  $C_0$  were 0.107, 0.128 and 0.132 microstrain/psi (15.52, 18.56 and 19.14 microstrain/MPa), respectively, for wires WE, WG and WH. Again the averages of six test measurements are shown in Figure 10 for each wire. While the prisms were aimed at a release strength of 6,000 psi (41.4 MPa), the actual release strength and other material properties varied from specimen to specimen [3], which may have contributed to the discrepancies observed in the surface strain profiles near the prism ends for specimens made with wires WG and WH (Figure 10).

**Table 2. Concrete and steel material parameters used in simulations of untensioned pullout and pretensioned prism tests.**

	Concrete		Steel
Young's modulus $E$	4,028 ksi (27.8 GPa)	Young's modulus	30,000 ksi (206.8 GPa)
Tensile strength $\sigma_{t0}$	478.8 psi (3.3 MPa)	Yield strength	274,000 psi (1,889.2 MPa)
Compressive strength $\sigma_{cu}$	5977.8 psi (41.2 MPa)		

**Table 3. Calibrated bond model parameters.**

Parameters	WE	WG	WH
$D_{nn}^e$	12,889,494 lbf/in <sup>3</sup> (3,498.8 N/mm <sup>3</sup> )		
$D_{ns}^e (= D_{nt}^e)$	268,531 lbf/in <sup>3</sup> (72.9 N/mm <sup>3</sup> )		
$u_{tc}^{pl}$	0.04 in. (1.02 mm)	0.04 in. (1.02 mm)	0.04 in. (1.02 mm)
$u_{td}^{pl}$	0.14 in. (3.56 mm)	0.17 in. (4.32 mm)	0.26 in. (6.60 mm)
$u_{ts}^{pl}$	0.15 in. (3.81 mm)	0.18 in. (4.57 mm)	0.27 in. (6.86 mm)
$a_0$	550 psi (3.79 MPa)	400 psi (2.76 MPa)	1000 psi (6.89 MPa)
$H_0$	0.0012 psi <sup>-1</sup> (0.174 MPa <sup>-1</sup> )	0.0022 psi <sup>-1</sup> (0.319 MPa <sup>-1</sup> )	0.001 psi <sup>-1</sup> (0.145 MPa <sup>-1</sup> )
$H_1$	0.0012 psi <sup>-1</sup> (0.174 MPa <sup>-1</sup> )	0.005 psi <sup>-1</sup> (0.725 MPa <sup>-1</sup> )	0.018 psi <sup>-1</sup> (2.611 MPa <sup>-1</sup> )
$\mu_d^{max}$	0.01	0.014	0.013

## VERIFICATION WITH TEST DATA

The FE bond models developed and calibrated in this paper were verified with concrete surface strain data measured on actual concrete crossties made at a plant [4]. The strain data read from Whittemore gauges were compared with FE simulation results. Figure 11 shows the end and symmetric side views of the concrete crosstie model used in the analyses. Like the prism model, the tie model was constructed for one eighth of the geometry due to symmetry. The concrete material, steel material and bond model parameters in Table 2 and Table 3 were applied. Again the measured concrete surface strains had significant creep components, and the FE predicted surface strains were adjusted with creep strains according to Eq. (30-32). Figure 12 compares the averages of six Whittemore gauge measurements with the creep adjusted FE strains for each wire. The estimated creep compliance parameters  $C_0$  were 0.173, 0.199 and 0.201 microstrain/psi (25.09, 28.86 and 29.15 microstrain/MPa), respectively, for wires WE, WG and WH. The simulation results agree reasonably well with the test data.

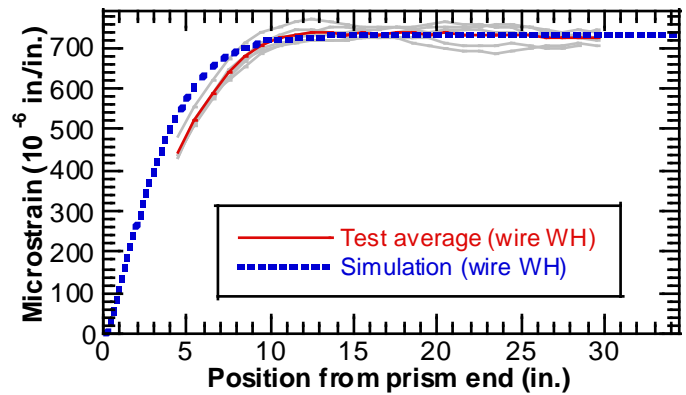
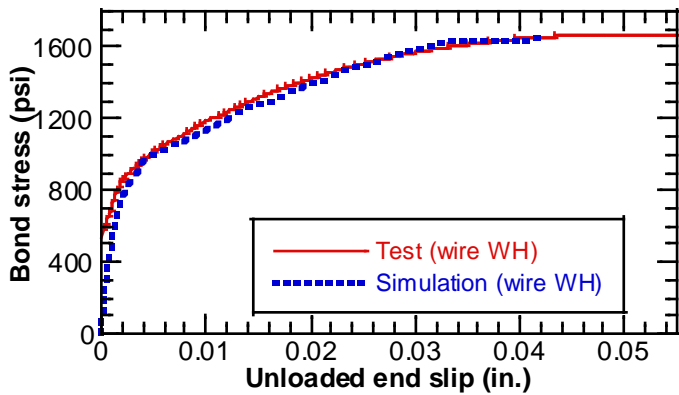
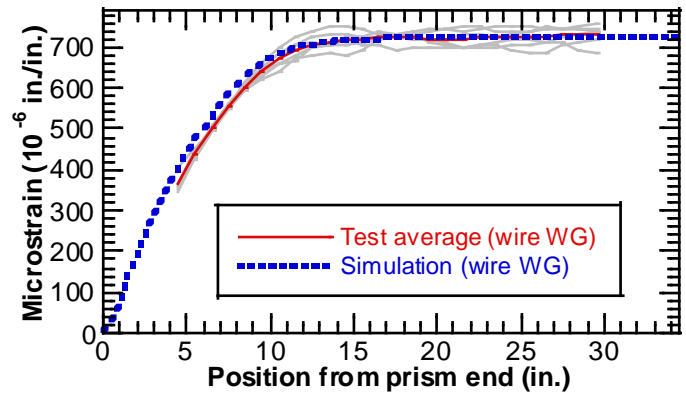
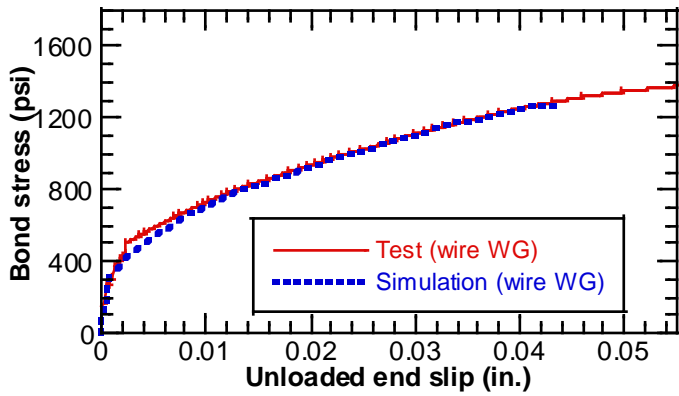
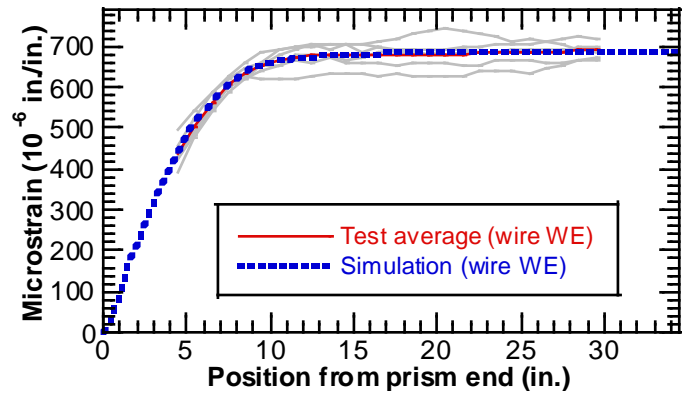
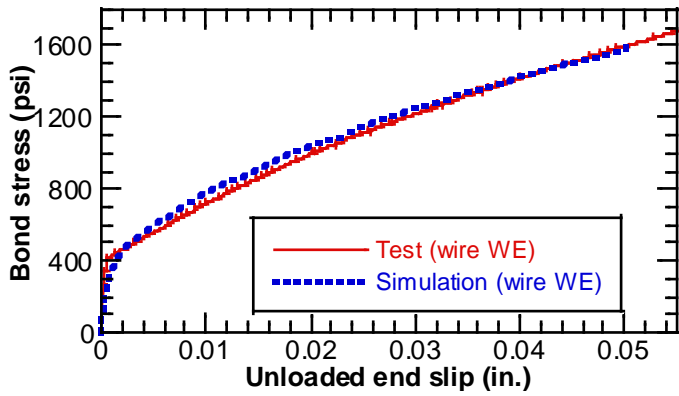


Figure 9: Bond stress-unloaded end slip curves: test versus FE results (1 psi = 6.89 MPa, 1 in. = 25.4 mm).

Figure 10: Measured versus FE predicted and creep adjusted surface strain profiles in concrete prisms (1 in. = 25.4 mm).

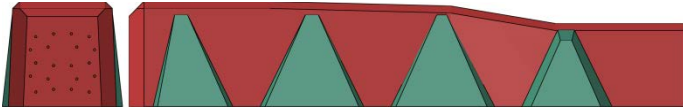


Figure 11: End and symmetric side views of the concrete cross-tie model.

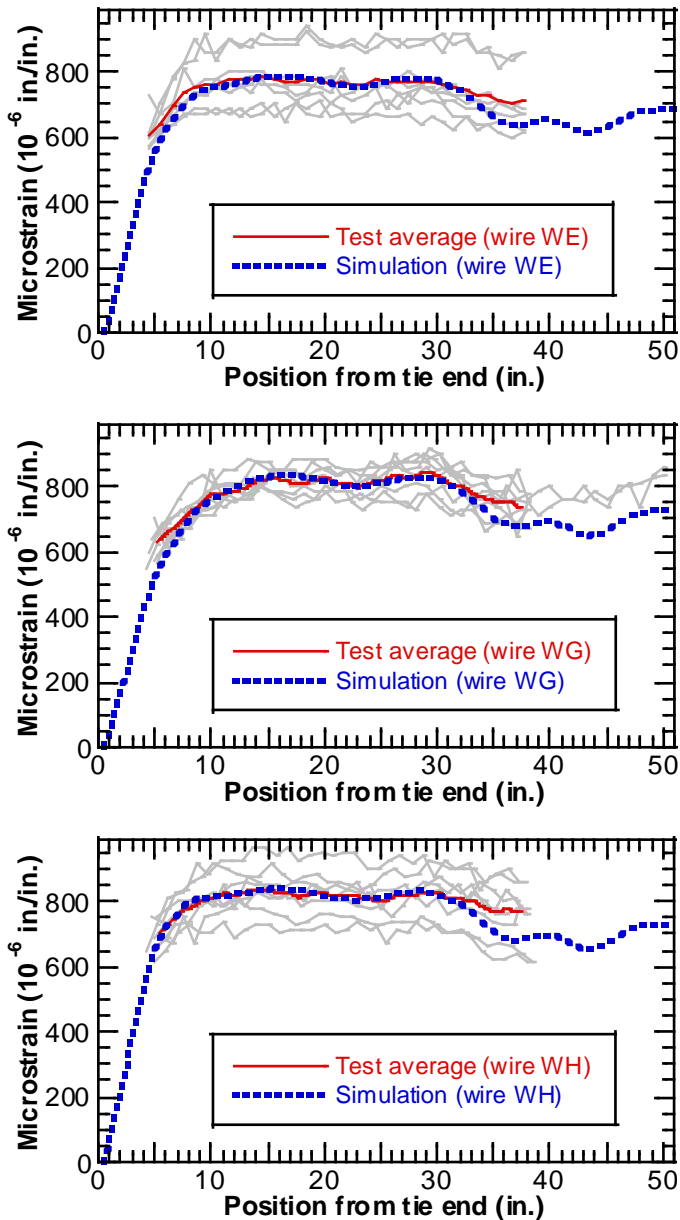


Figure 12: Whittemore gauge measurements versus FE predicted and creep adjusted surface strain profiles of plant made concrete cross-ties (1 in. = 25.4 mm).

## SUMMARY AND CONCLUSIONS

Elasto-plastic bond models were developed for the interfaces between three indented prestressing wires and concrete, which can be directly applied to FE analysis of railroad concrete cross-ties. The yield function is expressed as a quadratic function of shear stress and a linear function of normal stress.

The plastic flow is defined such that the plastic dilatation evolves with the plastic slip. The adhesive, hardening and dilatational bond model parameters were calibrated from laboratory wire pullout and pretensioned prism tests conducted on concrete specimens embedded with the three respective indented wires. The bond models were then verified with concrete surface strain profiles measured on actual concrete ties made in a plant with each of the three wires. With appropriate creep strain adjustments, the surface strain profiles predicted by the FE method agree reasonably well with the experimental measurements. Combined with the two previously developed bond models for a smooth wire and a seven-wire strand, the bond models for the indented wires in this paper constitute a comprehensive set of bond models now available for studies of concrete tie behavior.

## ACKNOWLEDGEMENT

The work described in this paper was sponsored by the Office of Research, Development and Technology, Federal Railroad Administration, U.S. Department of Transportation. Directions provided by Messrs. Gary Carr and Cameron Stuart of the Track Research Division are gratefully acknowledged. The authors would also like to thank Professors Robert J. Peterman and B. Terry Beck of Kansas State University for sharing the test data applied in this study.

## REFERENCES

- [1] Yu, H., Jeong, D., Marquis, B., and Coltman, M., 2015, "Railroad Concrete Tie Failure Modes and Research Needs," 2015 Transportation Research Board 94th Annual Meeting, TRB15-0311.
- [2] Arnold, M. L., Peterman, R. J., Bodapati, N. N. B., Beck, B. T., and Wu, C. H. J., 2013, "Development of a Standard Bond Test for Indented Prestressing Wires," Proc. 2013 Joint Rail Conference, JRC2013-2461.
- [3] Bodapati, N. N. B., Zhao, W., Peterman, R. J., Wu, C. H. J., Beck, B. T., Haynes, M., and Holste, J. R., 2013, "Influence of Indented Wire Geometry and Concrete Parameters on the Transfer Length in Pretensioned Concrete Cross-ties," Proc. 2013 Joint Rail Conference, JRC2013-2463.
- [4] Bodapati, N. N. B., Peterman, R. J., Zhao, W., Beck, B. T., Wu, C. H. J., Holste, J. R., Arnold, M. L., Benteman, R., and Schweiger, R., 2013, "Transfer-Length Measurements on Concrete Railroad Ties Fabricated with 15 Different Prestressing Reinforcements," Proc. 2013 PCI Convention and National Bridge Conference.
- [5] Zhao, W., Beck, B. T., Peterman, R. J., Wu, C. H. J., Bodapati, N. N. B., and Lee, G., 2014, "Reliable Transfer Length Assessment for Real-Time Monitoring of Railroad Cross-tie Production," Proc. 2014 Joint Rail Conference, JRC2014-3830, American Society of Mechanical Engineers.
- [6] Haynes, M., Wu, C. H. J., Beck, B. T., Bodapati, N. N. B., and Peterman, R. J., 2013, "Prestressing Steel Reinforcement Wire Bond Index Number," Proc. 2013

- Joint Rail Conference, JRC2013-2422, American Society of Mechanical Engineers.
- [7] Yu, H., and Jeong, D. Y., 2014, "Bond between Smooth Prestressing Wires and Concrete: Finite Element Model and Transfer Length Analysis for Pretensioned Concrete Crossties," Proceedings of the 2014 ASCE Structures Congress.
- [8] Yu, H., and Jeong, D.Y., 2015, "Finite Element Bond Models for Seven-Wire Prestressing Strands in Concrete Crossties," Proceedings of the 2015 Joint Rail Conference, JRC2015-5758.
- [9] Yu, H., Marquis, B., and Jeong, D.Y., "Failure Analysis of Railroad Concrete Crossties in Center Binding Conditions Using Finite Element Method," Proceedings of the Stephenson Conference, Institution of Mechanical Engineers, London, UK, April 21-23, 2015.
- [10] Yu, H., 2016, "Estimating Deterioration in the Concrete Tie-Ballast Interface Based on Vertical Tie Deflection Profile: A Numerical Study," 2016 Joint Rail Conference, JRC2016-5783.
- [11] Dassault Systèmes, 2012, Abaqus Analysis User's Manual.
- [12] Yu, H., Jeong, D. Y., Choros, J., and Sussmann, T., 2011, "Finite Element Modeling of Prestressed Concrete Crossties with Ballast and Subgrade Support." Proc. ASME 2011 International Design Engineering Technical Conferences & Computers and Information in Engineering Conference, DETC2011-47452.
- [13] Yu, H., and Jeong, D. Y., 2012, "Railroad Tie Responses to Directly Applied Rail Seat Loading in Ballasted Tracks: A Computational Study," Proc. ASME/ASCE/IEEE 2012 Joint Rail Conference, JRC2012-74149.
- [14] Zienkiewicz, O. C., and Taylor, R. L., 1991, The Finite Element Method. Vol. 2. Solid and Fluid Mechanics Dynamics and Non-Linearity, Fourth Edition, McGraw-Hill, London.
- [15] Michalowski, R., and Mroz, Z., 1978, "Associated and Non-Associated Sliding Rules in Contact Friction Problems," Archives of Mech., 30(3), pp. 259-276.
- [16] Bazant, Z. P., and Baweja, S., 2000, "Creep and Shrinkage Prediction Model for Analysis and Design of Concrete Structures: Model B3," ACI Special Publications, 194, pp. 1-84.